Title

Nanoconfinement of High Hydrogen-to-Metal Ratio Lanthanum Hydrides in Functionalized Carbon Hosts

Journal

ACS Applied Energy Materials, 8(1)

ISSN

2574-0962

Authors

Shivanna, Mohana

Elmslie, Timothy A

Spataru, Catalin D

et al.

Publication Date

2025-01-13

DOI

10.1021/acsaem.4c02100

Nanoconfinement of High Hydrogen-to-Metal Ratio Lanthanum Hydrides in Functionalized Carbon Hosts

Mohana Shivanna,[a] Timothy A. Elmslie,[a] Catalin D. Spataru,[a] Sakun Duwal,[a] Nicholas Porcellino,[b] Sergio Mouzaya,[b] Christopher P. Pakhanyan,[b] Farid El Gabaly,[a] Saori Kawaguchi-Imada,[c] Jinghua Guo,[d] Zengqing Zhuo,[d] Min-Jae Kim,[d] Blake T. Sturtevant,[e] Joseph A. Teprovich Jr.,[b] Mark D. Allendorf,[a] Peter A. Sharma,*[a] and Vitalie Stavila*[a]

[a]Sandia National Laboratories, Livermore, California 94550; Albuquerque, New Mexico 87185, USA

[b]California State University Northridge, Northridge, California 91330, USA

[c]Super Photon ring-8, 1-1-1 Kouto, Sayo-cho, Sayo-gun Hyogo 679-5198, Japan

[d]Advanced Light Source, Lawrence Berkeley National Laboratory, Berkeley, California 94720, USA

[e]Los Alamos National Laboratory, Los Alamos, New Mexico 87545, USA

KEYWORDS: metal superhydrides, lanthanum hydride, hydrogen storage, diamond anvil cell, nanoconfinement

ABSTRACT: Metal hydrides with a high hydrogen content are important for materials-based hydrogen storage and high-temperature superconductivity. Nanoconfinement of metal hydrides in porous hosts is a promising strategy to tune thermodynamic stability and control the hydrogen-to-metal ratio. However, lanthanum hydride (LaH_x) nanoconfinement in porous materials has been limited due to the challenges associated with isolating and stabilizing nanoparticles of La or La-hydrides. Here we successfully demonstrated the chemical reduction of La(III) salts to La(0), and subsequent infiltration into pure CMK-3 and nitrogen-doped CMK-3 (NCMK-3) porous carbons. Transmission electron microscopy measurements revealed a uniform distribution of LaH_x species within the carbon hosts, while X-ray absorption spectroscopy and X-ray photoelectron spectroscopy provided detailed information about the local chemical environment. Sieverts measurements indicate that LaH_x@NCMK-3 could desorb up to 0.75 wt % hydrogen, which is higher than non-nitrogen functionalized CMK-3 (0.43 wt% H). Density Functional Theory and *ab initio* molecular dynamics calculations indicate that host-guest interaction energies are favorable for porous carbon with nitrogen defects, which is supported by experimental evidence. Moreover,

high-pressure synchrotron X-ray diffraction measurements were conducted using a diamond anvil cell up to 60 GPa and reveal that the nitrogen-functionalized nanoporous carbon host favors the formation of higher H:La ratios in presence of ammonia borane compared to the pure CMK-3 host. This approach could serve as a suitable platform for developing nanoscale superconducting materials at lower pressures and temperatures compared to bulk.

1. INTRODUCTION

Metal hydrides with high hydrogen-to-metal ratio are used in various applications, such as hydrogen storage,[1] thermal energy storage,[2] Li-ion battery anodes,[3] and solid-state ion electrolytes.[4] Rare earth metal hydrides have been intensively studied since 1950's due to their ability to undergo reversible hydrogen absorption and desorption and unusual properties function of hydrogen-to-metal ratio.[5] Lanthanum films can reversibly absorb and desorb hydrogen,[6] a process that is accompanied by metal-insulator transitions and switchable optical behavior.[7] Hydrogenation of lanthanum typically does not proceed all the way to stoichiometric LaH_3 (2.13 wt% H),[7] but rather leads to sub-stoichiometric LaH_{3-x} *fcc* phases, with x depending on the hydrogenation conditions and reaction time.[8] Neutron powder diffraction, neutron vibrational spectroscopy, and quasielastic neutron scattering measurements reveal pressure-dependent H–H interactions in the octahedral and tetrahedral sites of the *fcc* lattice.[8] Hydrogen isotherm measurements in the La-H_2 system revealed a high thermodynamic stability, with measured values of ΔH = 207 kJ mol^{-1} H_2 and ΔS = 151 J mol^{-1} H_2.[9] The high thermodynamic stability makes lanthanum hydrides not ideal for near-ambient hydrogen storage but potentially suitable as hydrogen getters[10,11] and for high-temperature thermal energy storage applications.[2,12,13]

Recently, hypervalent lanthanide metal hydrides (also referred to as "superhydrides") have garnered significant attention for their potential as near-ambient temperature superconductors, a possibility initially derived from theoretical predictions and subsequently corroborated by experimental findings.[14] This potential relies on the concept of chemical compression provided by metal hydrides, which could form a hydrogen clathrate structure approaching the density of metallic hydrogen.[15, 16] The large chemical compression (> 100 GPa) leads to the formation of a dense hydrogen clathrate structure, with a strong electron-phonon coupling driven by phonon

softening caused by Fermi surface nesting, thus scattering electrons to form a Boze condensate composed of Cooper electron pairs.[17] The superconductivity was predicted computationally and experimentally validated in a number of hypervalent lanthanide hydrides using diamond anvil cell (DAC) techniques, including LaH_{10},[14] YH_9,[18] CeH_9,[19] LaH_6,[18] and YH_6.[20]

Lanthanum superhydrides are particularly promising for high-temperature superconductivity due to high H/La ratios that could be stabilized in a clathrate lattice. Calculations reveal that the high phonon frequencies of hydrogen atoms (part of the anionic sublattice of lanthanum superhydrides) significantly enhance electron-phonon coupling,[21] a key requirement for superconductivity. Several groups have successfully synthesized the superconducting *fcc*-LaH_{10} phase by laser heating La metal with pure hydrogen or ammonia borane (NH_3BH_3) at high pressure in a diamond anvil cell. The formation of superconducting LaH_x with T_c at 215 K and 150 GPa was observed by Drozdov *et al*.[14] by heating a sample of La in pure hydrogen just below 1000 K at 170 GPa. Somayazulu *et al*.[18] reported the superconducting lanthanum superhydride with T_c ~260 K at 180–200 GPa using NH_3BH_3 as the hydrogen source. Subsequently, Drozdov *et al*. changed the synthesized conditions and reported that LaH_{10} had a highest T_c of 250 K at 170 GPa.[14] In their work, they also confirmed the crystal structure of bulk LaH_{10} adopts a $Fm\bar{3}m$ space group via synchrotron X-ray diffraction and observed well-defined isotope effects. Besides those two groups, Hong *et al*. reported a T_c value of 246 K at 136 GPa,[22] and Sun *et al*. found that T_c decreased to 191 K as the pressure dropped from 138 to 120 GPa, which was associated with a $Fm\bar{3}m$ to C2/*m* phase transition.[23]

Recent research has demonstrated that transitioning from bulk to nanoscale dimensions can significantly impact the metal-hydrogen interactions by decreasing diffusion lengths, exploiting stress effects, reducing nucleation barriers, and modifying interface energies.[1,24] In addition, we previously showed that metastable metal hydrides such as $LiAlH_4$[25] and AlH_3[26] can be thermodynamically stabilized when confined inside the pores of functionalized scaffolds or hosts, reducing the pressure requirement for hydrogenation by orders of magnitude. Based on these observations, we hypothesize that nanoconfinement inside nitrogen-functionalized pores of NCMK-3 could lead to the formation of hypervalent lanthanide hydride phases (LnH_x; $x > 3$) at lower pressures than in bulk materials. Here, we present a chemical method for synthesizing lanthanum hydride (LaH_x) nanoparticles (NPs) using a lithium naphthalenide (Li-Nap) mediated reduction of LaI_3,[27] followed by hydrogenation of La NPs to form LaH_x. We show that it is possible

to confine these particles inside the pores of CMK-3 and NCMK-3 using wet-chemistry approaches. Our experiments and calculations indicate that nitrogen doping in NCMK-3 favors a higher H:La ratios upon compression in a diamond anvil cell, suggesting that significant charge transfer interactions occur between the nitrogen dopant of the carbon scaffold and LaH_x NPs.

2. RESULTS AND DISCUSSION

Synthesis and characterization. The synthesis of lanthanum NPs is performed using a method first described by Bartenbach *et al.* by reacting freshly prepared Li-naphthalenide (Li-Nap) with a solution containing LaI_3 in tetrahydrofuran (THF).[27] The solution mixture was allowed to sit overnight to ensure a complete reaction with LaI_3 and the formation of La NPs. The NPs are isolated by centrifugation and washed twice under an inert atmosphere with dry THF to remove unreacted species. The resting black solid was dried under vacuum at 80 °C and then hydrogenated at 100 bar H_2 at 350 °C for 12 hours to obtain the LaH_x NPs. The LaH_x@CMK-3 and LaH_x@NCMK-3 were prepared by mixing a 1:1 mass ratio of LaI_3 and the porous carbon in THF. To ensure dispersion of the LaI_3 in the porous carbon, the solution was sonicated for 10 minutes while maintaining an inert atmosphere. The subsequent steps of the process are the same for the formation of LaH_x NPs as described above. This procedure allows the synthesis of small size La NPs (<5 nm), which can be confined inside carbon pores.

The successful incorporation of LaH_x into the pores of CMK-3 and NCMK-3 was confirmed by several bulk and surface-sensitive characterization techniques. The transmission electron microscopy (TEM) measurements revealed that La-hydride particles were distributed uniformly in both host materials, CMK-3 and NCMK-3 (**Figure 1a,b**). The powder X-ray diffraction (XRD) patterns were measured to verify the crystallinity and phase purity for LaH_x NPs, carbon-infiltrated LaH_x samples, and compared with the bulk LaH_x material, as shown in **Figure 1c**. LaH_x species were found in the form of rod-shaped particles upon infiltration in CMK-3, whereas in the case of NCMK-3 spherical particles were observed. Such spherical LaH_x NPs have also been isolated separately (see TEM images in **Figures S1-2**). The XRD pattern for LaH_x NPs and infiltrated samples aligned with the pattern for bulk La-hydride, but showed significant peak broadening compared to bulk. This is expected due to the smaller crystallite sizes present in the NP samples versus bulk. Thermo-gravimetric analysis (TGA) was performed for both LaH_x@CMK-3 and

LaH_x@NCMK-3 as shown in **Figure S3-4**. As-synthesized materials were found to be stable up to ~350 °C based on the second plateau. From RT to 150 °C (LaH_x@NCMK-3) and from RT to 200 °C (LaH_x@CMK-3), a small weight gain was observed, presumably due to a reaction with trace amounts of moisture during the measurement.

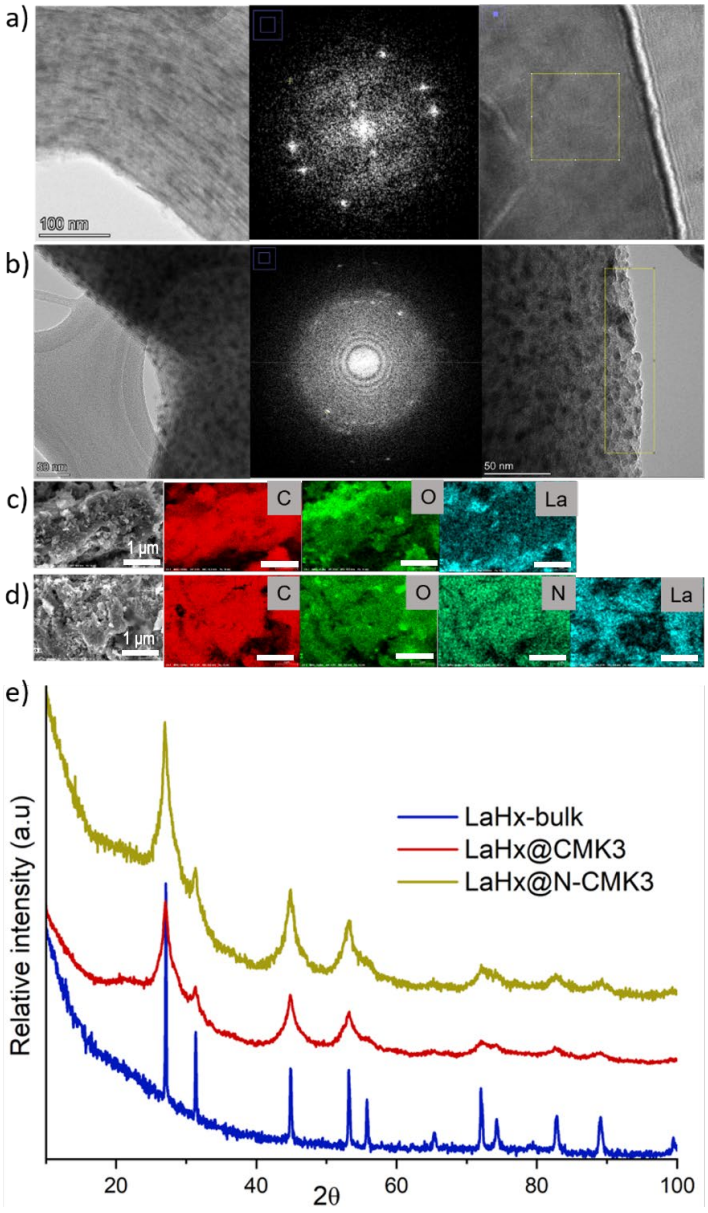

Figure 1. a) TEM images for LaH_x@CMK-3 showed that LaH_x species infiltrated in the form of rod shape (left), and electron diffraction for the selected region of the image (middle and right). b) While in the case of NCMK-3, LaH_x species are in the form of a sphere shape (left), electron diffraction pattern for the selected region of the image (middle and right). c) Elemental EDS mapping of C, O,

and La in LaH_x@CMK-3. d) C, O, N and La EDS maps in LaH_x@NCMK-3, showing the metal evenly distributed within the host material. e) PXRD diffraction measured for LaH_x@CMK-3 and LaH_x@NCMK-3 compared with bulk LaH_x.

To determine the Brunauer−Emmett−Teller (BET) surface area[15] and total pore volume before and after nanoconfinement, N_2 isotherms were measured at 77 K (**Figure 2**). These results indicate a significant reduction in the BET and pore volume upon incorporation of the LaH_x NPs into the carbon scaffold materials. Additionally, the isotherm profiles for both the host materials and the LaH_x-infiltrated samples reveal a substantial mesoporous character.[16] Upon infiltration, the BET surface area (301 m^2/g) and pore volume (0.58 cm^3/g) for LaH_x@CMK-3 is significantly reduced when compared to pure CMK-3, which has a surface area of 859 m^2/g and a pore volume of 1.15 cm^3/g. Similarly, a large reduction in the BET and pore volume was observed for LaH_x@NCMK-3 (~44 m^2/g and 0.09 cm^3/g) versus NCMK-3 (741 m^2/g and 0.64 cm^3/g). The reduction in pore volume and BET surface area are consistent with other hydrides inflitrated in CMK-3 and NCMK-3.[25,28]

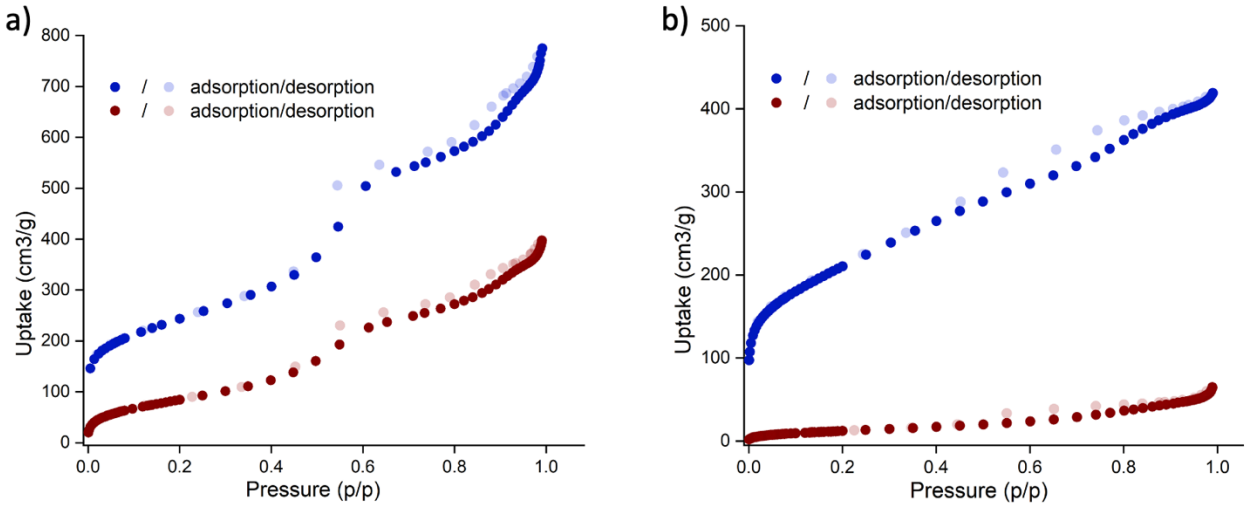

Figure 2. N_2 sorption isotherms measured at 77 K for a) CMK-3 (blue) and LaH_x@CMK-3 (red) and b) NCMK-3 (blue) and LaH_x@NCMK-3 (red). The lighter data points represent desorption data, while the darker data points indicate absorption data.

Surface-sensitive X-ray photoelectron spectroscopy (XPS) measurements provide clear evidence that several distinct nitrogen functionalities are present in NCMK-3 (**Figure S5**). Pyridinic N (50%), pyrole N (32%) and pyridone N (19%) are the main functional groups on the surface of the NCMK-3, with minor contributions from oxidized species (**Figures S5-7**). This is good agreement with the reported literature for different nitrogen species observed in NCMK-3.[29] After LaH_x confinement, the amount of nitrogen functionalities slightly varied, pyridinic N (45%), pyrrolic N (46%), and oxidized N (9.4%). X-ray absorption spectroscopy (XAS) measurements (**Figures S8-9**) reveal two major K-edge N peaks which correspond to pyridinic and pyrrolic nitrogens.[30] The main peak for pyridinic nitrogen is significantly shifted to higher energy for LaH_x@NCMK-3 compared to NCMK-3, which is consistent with the previouly reported work in which Li-N chemical interaction leads to an energy shift in $LiAlH_4$@NCMK-3.[25] This supports the conclusion that there exist strong chemical interactions between nitrogen and LaH_x clusters. For lanthanum in LaH_x@CMK-3 and LaH_x@NCMK-3, the two prominent signals correspond to the M5 and M4 edges of 3*d* to 4*f* transitions (**Figure S9**).[31]

Elemental analysis was performed for CMK-3 and NCMK-3 materials before and after LaH_x nanoconfinement (**Table S1**). For these measurements, the samples were kept in vacuum at 80 °C overnight to remove volatiles.

The elemental analysis for CMK-3 (C: 91.72%, H: 0.84%) and NCMK-3 (C: 68.30%, H: 1.68%, N: 20.73%) provides the composition of the starting host materials. The compositions for LaH_x@CMK-3 (C: 47.97%, H: 1.46%, La: 26.0%) and LaH_x@NCMK-3 (C: 41.05%, H: 2.24%, N: 3.08%, La: 24.8%) show an increase in hydrogen content in the infiltrated samples, attributed to hydrogen bound to lanthanum hydride. A slight variation in LaH_x loading between CMK-3 and NCMK-3 is within the experimental error of the analysis. Additionally, the significant difference in nitrogen content between NCMK-3 containing samples before and after LaH_x infiltration is likely due to partial nitrogen desorption during the activation process (performed at 200 °C in vacuum for 5 hours). EDS measurements confirmed the presence of nitrogen in LaH_x@NCMK-3, as shown in **Figure 1d**.

Hydrogen adsorption and desorption. To test the hypothesis that nanoconfinement and the local pore environment influence the hydrogen desorption properties of LaH_x, we conducted Sieverts measurements to determine the amount of hydrogen released, and residual gas analysis (RGA) to verify the purity of desorbed hydrogen (**Figure 3 and S10-11**). For these measurements, the

LaH_x@CMK-3 and LaH_x@NCMK-3 were evacuated at 80 °C overnight to remove residual volatiles. About 150 mg of powder was loaded into a stainless-steel sample holder under an inert atmosphere. The amount of hydrogen desorbed was measured upon heating the sample from RT to 370 °C. For LaH_x@CMK-3, the desorption kinetics are found to be faster until the temperature reaches 370 °C, after which it slows and remains steady while the temperature is maintained at 370 °C. After 10 hours of heating at 370 °C, the total amount of hydrogen desorbed from LaH_x@NCMK-3 was 0.43 wt% (**Figure 3a**), while LaH_x@NCMK-3 desorbed 0.75 wt% hydrogen under the same conditions (**Figure 3b**), clearly indicating a greater hydrogen release when nitrogen-functionalized NCMK-3 is used as a scaffold. Interestingly, the hydrogen release from LaH_x@NCMK-3 features a fast step, followed by more sluggish hydrogen release (**Figure 3b**).

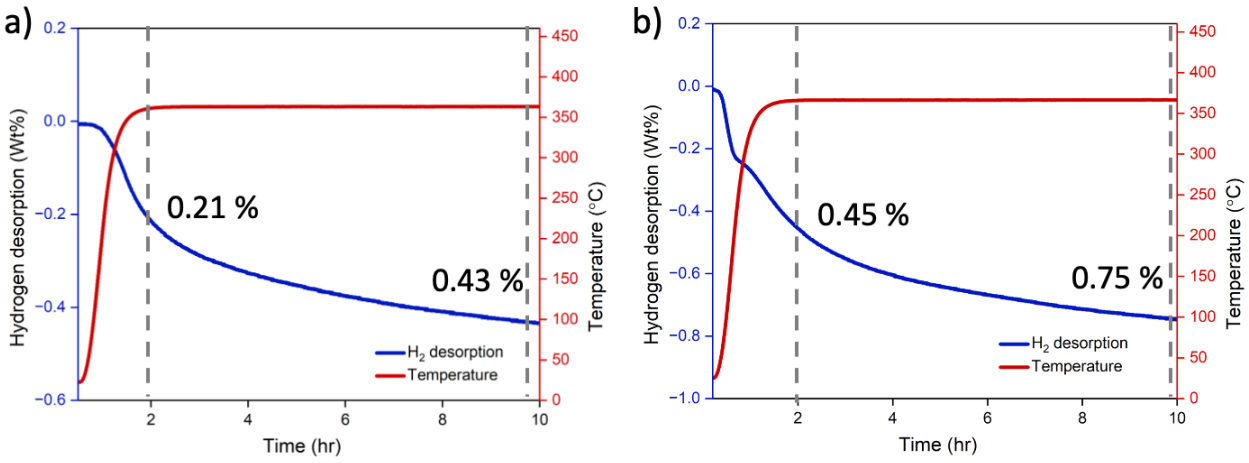

Figure 3. Sieverts measurements for LaH_x@CMK-3 (a) and LaH_x@NCMK-3 (b) to confirm the hydrogen wt% desorption with increase in temperature.

The presence of nitrogen functionality enhances the La loading and thereby enables a higher weight % H in the case of LaH_x@NCMK-3. This indicates that charge transfer and nano-confinement enable the high capacity and faster kinetic hydrogen desorption which is consistent with the XAS and other spectroscopy measurements of nitrogen changes. To probe the reversibility, we performed a second desorption cycle after rehydrogenation at 100 bar H_2 and 300 °C for two hours. The subsequent hydrogen desorption was measured for both LaH_x@CMK-3 and LaH_x@NCMK-3 and revealed a similar wt% hydrogen released as on the first cycle (**Figure S10**). Sieverts measurements were also performed on both pure CMK-3 and NCMK-3, revealing minimal

hydrogen desorption (<0.1 wt%) when heated to 360 °C for 10 hours (**Figure S11**). This suggests that the primary contribution to the observed reversible capacity is due to hydrogen desorption from lanthanum hydride.

To probe the composition of the gaseous mixture released, RGA-MS measurements[17] were conducted isothermally in the temperature range from 100 to 300 °C in 50 °C steps (**Figure S12**). The gas released from LaH_x@NCMK-3 at low temperatures is primarily H_2, indicating no decomposition of the host materials up to 300 °C. Other peaks at 18 (*m/z*) and 32 (*m/z*) that correspond to trace amounts of H_2O and O_2 are present in the RGA-MS lines (**Figure S12b**). The peak at 28 (*m/z*) belongs to nitrogen, which is flow gas used in the RGA measurement. Both H_2O and O_2 originated from the line stream connected to the RGA setup. The same range of *m/z* peaks was observed for LaH_x@CMK-3 that correspond to H_2, H_2O, O_2, and N_2 as shown in **Figure S12a**. In both samples, we also found other small peaks of *m/z* at 14 may correspond to double-ionized nitrogen. This analysis further verified that the hydrogen weight % desorbed during the Sieverts measurements corresponds to pure hydrogen and is not associated with impurities or other volatiles.

High pressure DAC measurements. In order to understand the pressure dependent behavior of LaH_x@CMK-3 and LaH_x@NCMK-3 in the presence of an external hydrogen source we conducted X-ray diffraction (XRD) measurements using diamond anvil cells (DAC) at the SPring-8 synchrotron facility.[32] Small amounts (few μg) of sample were loaded into DACs in Re gaskets between diamonds with 300 μm culets. Gold powder was loaded alongside the samples as a pressure sensor. Ammonia borane (NH_3BH_3)[33, 34] was used as an external hydrogen source (10:1 NH_3BH_3:sample molar ratio). The XRD measurements were collected while gradually increasing pressure up to 45-60 GPa, depending on the sample. DIOPTAS software[35] was used to process raw .tif files generated during data collection into a format readable by GSAS-II, and GSAS-II[36] was used for phase identification and Rietveld refinement of powder XRD patterns. This analysis shows that LaH_x@CMK-3, LaH_x@CMK-3+NH_3BH_3, and LaH_x@NCMK-3, exist in an I4/mmm (tetragonal lattice) structure up to 46, 46, and 57 GPa, respectively (**Figures 4** and **5**) with no signs of structural transition. The pattern for LaH_x@NCMK-3+NH_3BH_3 differs from the other three samples, possessing a $P6_3/mmc$ structure (hexagonal lattice) (**Figure S13**). The pressure versus volume per La atom plot indicates that the LaH_x@CMK-3 sample has the lowest volume per La.

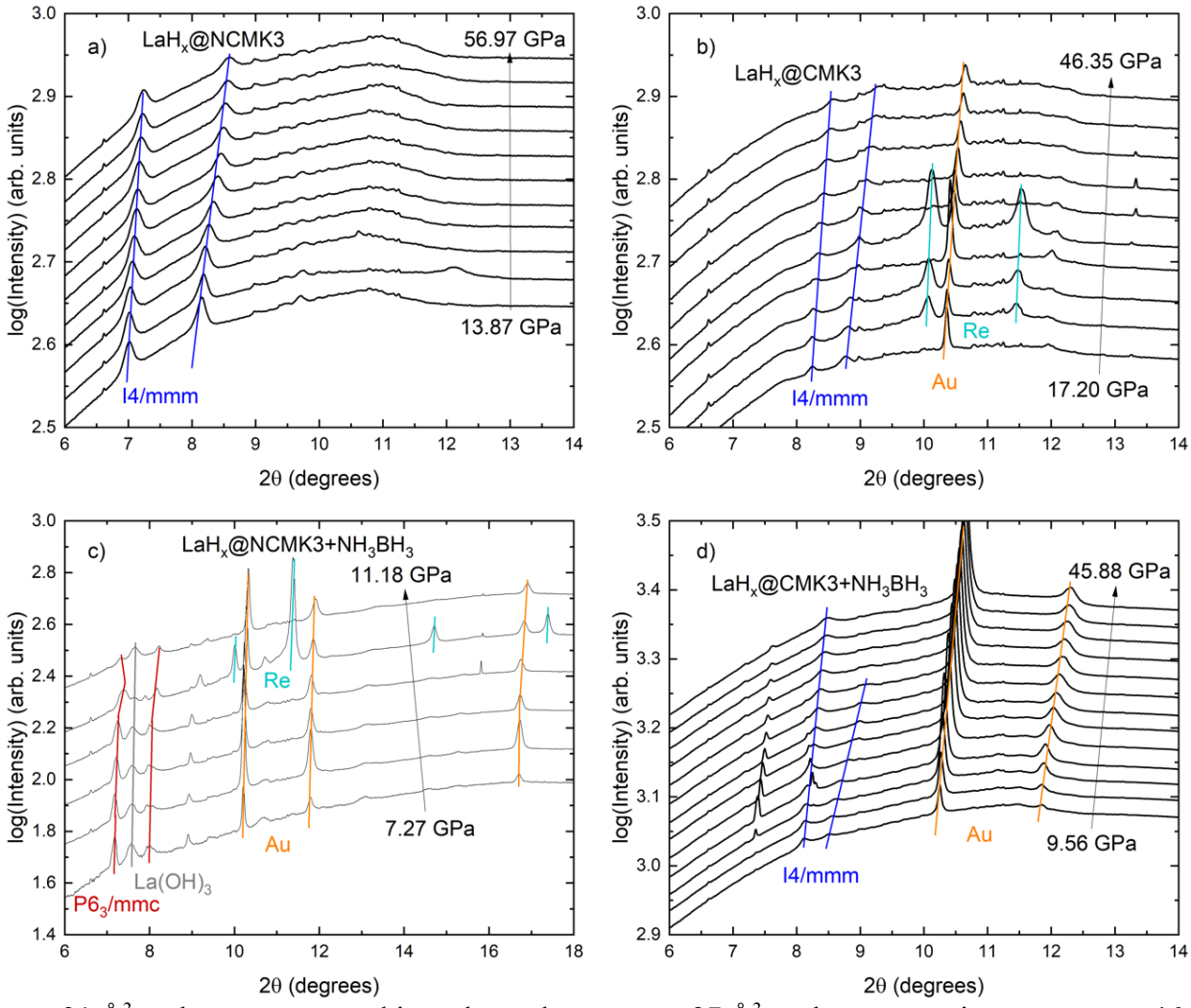

atom, 31 Å^3, at low pressure and its volume decreases to 27 Å^3 as the pressure increases up to 46 GPa (**Figure 4a and S14**).

Figure 4. Diamond anvil cell XRD patterns arranged from low to high pressure for a) LaH_x@NCMK-3, b) LaH_x@CMK-3, c) LaH_x@NCMK-3+NH_3BH_3, d) LaH_x@CMK-3+NH_3BH_3. Pressure increases with increasing y-axis offset, and the intensities are offset for clarity.

The same trend was observed in the presence of NH_3BH_3, but with slightly higher volume per La, 33 to 29 Å^3, at pressures up to 46 GPa. For LaH_x@NCMK-3 without NH_3BH_3, the volume per La atom is higher compared to LaH_x@CMK-3 and LaH_x@CMK-3+NH_3BH_3, as the pressure is increased up to 57 GPa. This data is comparable to work reported by Laniel *et al*[37] for LaH_3, 31.5

Å^3 at 50 GPa. In another study, LaH_2 has been studied using DAC up to ~22 GPa, leading to a decrease in the volume per La atom from 45 to 36.3 Å^3.[38] We found the pressure dependent behavior of LaH_x@NCMK-3+NH_3BH_3 to be significantly different from the other samples. The volume per La atom was 47 Å^3 at 7 GPa and decreased to 43 Å^3 at 11 GPa (**Figure 5a and S13**). Unfortunately, further increases in pressure beyond 11 GPa lead to amorphization and difficulty in accurately refining the PXRD patterns. We also compared this pressure dependent behavior of these samples to other reported work as shown **Figure S13**.[39] This verified that the presence of nitrogen functional groups in NCMK-3 hosts with or without NH_3BH_3 enhances the higher hydrogen content compared to pure bulk lanthanum or bulk lanthanum hydrides. The conversion of volume per La atom to number of hydrogen atoms is plotted in **Figure 5b** using a simplified method of subtracting the per-atom volume of elemental La and then dividing by the per-atom volume of elemental H_2 at a given pressure (see more details in Supporting Information). The estimated hydrogen concentration in LaH_x@CMK-3 was higher than LaH_x@CMK-3+NH_3BH_3 in the pressure range from 17 to 46 and 9.5 to 46 GPa, respectively. The LaH_x@NCMK-3 sample showed a hydrogen content while increase in the pressure range from 14 to 49 GPa compared to LaH_x@CMK-3 and LaH_x@CMK-3+NH_3BH_3. For LaH_x@NCMK-3+NH_3BH_3, a much higher hydrogen content observed at 7 GPa, which increases up to 11 GPa. The fact that all shown datasets, including those without a hydrogen source, have a positive slope demonstrates that this compound is less compressible than the elemental volumes alone would imply. The higher values observed in nitrogen-doped samples suggest that nitrogen dopants promote the formation of a higher hydrogen-to-metal ratio compared to carbon hosts without nitrogen.

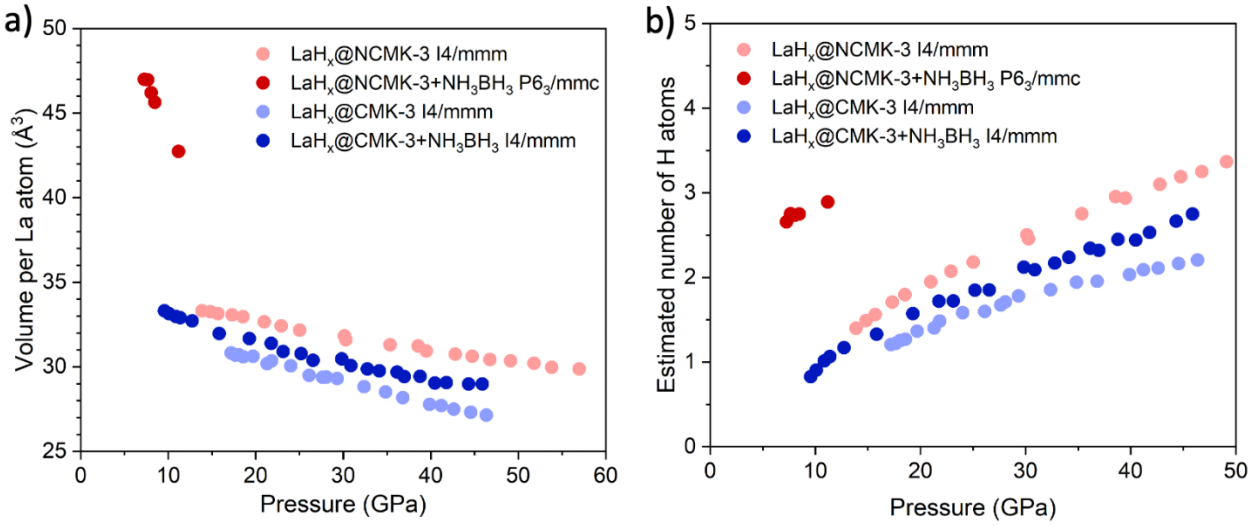

Figure 5. High-pressure synchrotron XRD measurements, with pressure plotted on the x-axis, and volume per La atom (a) or estimated hydrogen atoms per La (b) on the Y-axis for LaH_x@CMK-3, LaH_x@CMK-3+NH_3BH_3, LaH_x@CMK-3, and LaH_x@NCMK-3+NH_3BH_3.

Theoretical calculations and atomistic insights. To rationalize the observed higher hydrogen-to-metal ratio in the presence of nitrogen defect, density functional theory (DFT) and *ab initio* molecular dynamics (AIMD) calculations[13] were performed with the VASP code[40] in conjunction with projector augmented wave (PAW) pseudo-potentials (see also Supplemental Materials).[41] The calculations were conducted by anchoring $(LaH_3)_n$ clusters of different sizes (n=8,13) on a graphene sheet with two types of pyridine nitrogen defects (**Figure 6**). We then compared them with pure graphene without nitrogen defects to calculate the difference in energies. The structures were equilibrated for ~10 ps with 1 fs time steps and then quenched to 0 K by relaxing the forces to less than 0.05 eV/Å. The same setup was used for isolated clusters and graphene with and without defects. The host-guest interaction energies are more favorable for $(LaH_3)_8$ cluster by -5.4 eV and -6.2 eV in 4X1N and 4X2N sites compared to graphene without nitrogen, respectively. Similarly, for the $(LaH_3)_{13}$ cluster, the energy gain was found to be -5.8 eV and -6.9 eV for graphene with 4X1N and 4X2N sites (**Figure 6**), revealing that strong charge transfer interactions occur between porous carbon host and LaH_x clusters in the presence of nitrogen. These calculations further support experimental studies, which showed that high-pressure DAC measurements and Sieverts data suggest a higher wt % of hydrogen desorption for carbon hosts with nitrogen defects.

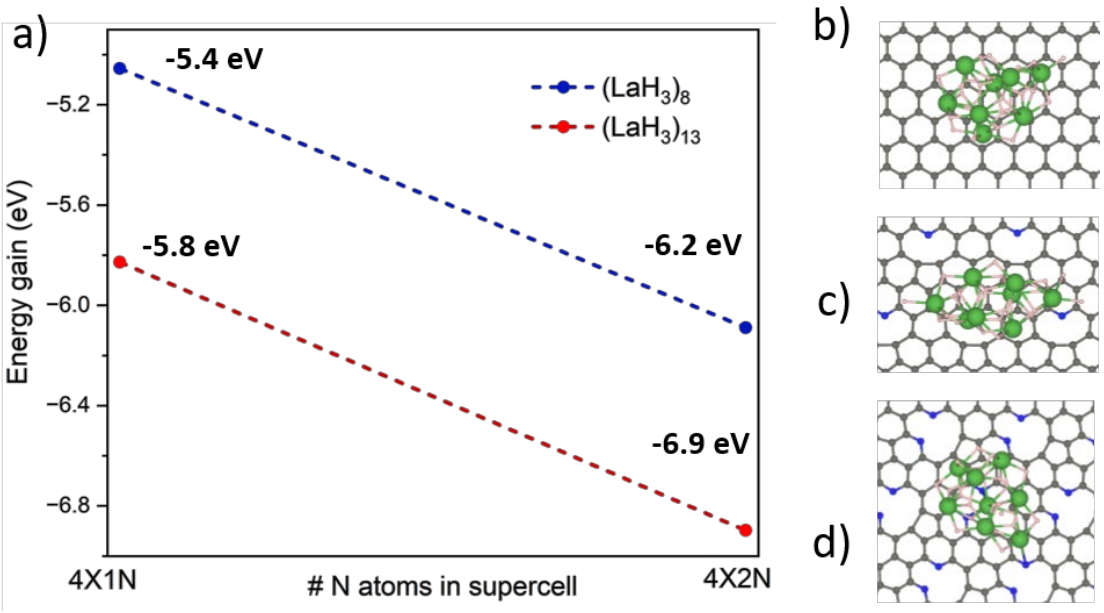

Figure 6. Energy calculations for different LaH_3 clusters on graphene and graphene with pyridinic defects. a) The energy gain observed for pyridine functionality over no nitrogen defects. Interactions of $(LaH_3)_8$ or $(LaH_3)_{13}$ cluster with the nitrogen-functionalized carbon at 4X1N and 4X2N sites. b, c, and d) $(LaH_3)_8$ clusters encored on graphene, graphene with 4X1N, and graphene with 4X2N, respectively.

To understand why $(LaH_3)_x$ clusters bind near a pyridinic defect we have calculated the planar-averaged charge density difference between the $(LaH_3)_8$ cluster adsorbed on a substrate (graphene or graphene with a single pyridinic defect) and the isolated subsystems. The redistribution of electron density and the cumulative charge are depicted in **Figure S15** as a function of the distance along the direction perpendicular to the substrate (z-axis). The substrate is located around z=3 Å while the cluster is located at z >5.5 Å (**Figure S15a**). The plots indicate that there is electron transfer taking place upon adsorption from the cluster towards the substrate. We note that in the case where the substrate is graphene with a pyridinic defect (1x1N), there is more charge transferred from the cluster to the substrate/cluster interface compared to graphene alone. Specifically, **Figure S15b** reveals increased electron density accumulation (around 4.5 Å) between the pyridinic defect and the cluster, indicating a stronger interfacial interaction. This

provides a possible explanation for the larger energy gain seen in **Figure 6** for the $(LaH_3)_x$ clusters adsorbed on graphene with pyridinic defects.

3. CONCLUSIONS

We demonstrated the successful nanoconfinement of LaH_x using a synthetic method which involves reducing lanthanum salts with Li-naphthalenide and infiltrating the resulting La NPs within the pores of CMK-3 and nitrogen-functionalized NCMK-3. The La NPs can be reversibly hydrogenated and dehydrogenated, with the LaH_x@NCMK-3 sample desorbing 0.75 wt% H compared to 0.43% desorbed from LaH_x@CMK-3. Electron microscopy measurements confirm that LaH_x NPs can diffuse deep into the pores, indicating that LaH_x ($x<3$) NPs are distributed uniformly throughout the pores of CMK-3 and NCMK-3 but in different crystalline space groups depending on the host functionality. The BET-surface area measurements are consistent with TEM measurements and show a large reduction in the pore volume and surface area upon infiltration compared to empty hosts. Similar trends have been reported for porous materials that are confined with other metal hydrides.[25, 26, 42]

XAS, XPS, and elemental analysis were used to characterize the compositions, probe the nanoconfinement of LaH_x, and elucidate the effects of carbon functionality. The XPS and XAS data confirm the presence of nitrogen pyridine, pyrole and pyridone groups in NCMK-3 samples, which interact with La-hydride species. High-pressure DAC measurements revealed that LaH_x@NCMK-3 more readily takes up hydrogen vs. LaH_x@CMK-3, as well as vs. bulk lanthanum hydrides. The highest H:La ratio was observed in LaH_x@NCMK-3 upon compression to 49 GPa, believed to occur through hydrogen transfer from the host NCMK-3 to LaH_x. Our DFT calculations revealed that the interaction energies of LaH_x clusters are favorable towards graphene with nitrogen defects compared to pure graphene, aligning with previous studies on other hydrides.[43] Thus, energy gains of -5.8 eV $(LaH_3)_{13}$ and -5.4 eV $(LaH_3)_8$ were observed at 4X1N sites compared to binding to graphene without nitrogen functionality. The calculations and experiments support the hypothesis that nitrogen doping is critical to achieving higher hydrogen-to-metal ratio in La-hydrides compared to undoped CMK-3. The presence of nitrogen dopants in carbon hosts results in significant charge transfer interactions with metal hydride NPs, enhancing the local binding.[25, 44]

These results indicate that nitrogen-functionalized carbon host materials are suitable candidates for confining metal hydrides and enabling a high hydrogen-to-metal ratio. This strategy provided new insights about behaviors of LaH_x upon reducing the size of particles to the nano regime within a porous material. Although no superconducting phases could be stabilized at pressures up to 60 GPa, this approach proved useful in controlling the hydrogen-to-lanthanum ratio,[45, 46] which is a key feature in achieving low temperature superconductivity,[23,47] but also semiconducting behaviour.[48] This synthetic methodology could be potentially expanded to control the size of other rare-earth hydrides.[27,49] Moreover, this study indicates that superhydride phases could be created under milder conditions via nanoconfinement in nitrogen-functionalized host materials, rather than relying on synthesis methods that use bulk metals or metal hydrides.

ASSOCIATED CONTENT

Supporting Information. Additional experimental details, TGA-RGA, high pressure XRD fitting and data. This material is available free of charge via the Internet at pubs.acs.org.

AUTHOR INFORMATION

Corresponding Authors

Vitalie Stavila – Sandia National Laboratories, Livermore, California 94550, USA; Email: vnstavi@sandia.gov

Peter A. Sharma – Sandia National Laboratories, Albuquerque, New Mexico 87185, USA; Email: pasharm@sandia.gov

Authors

Mohana Shivanna – Sandia National Laboratories, Livermore, California 94550, USA

Timothy A. Elmslie – Sandia National Laboratories, Albuquerque, New Mexico 87185, USA

Catalin D. Spataru – Sandia National Laboratories, Livermore, California 94550, USA

Sakun Duwal – Sandia National Laboratories, Albuquerque, New Mexico 87185, USA

Nicholas Porcellino – Department of Chemistry and Biochemistry, California State University Northridge, 18111 Nordhoff St. Northridge, California 91330, USA

Sergio Mouzaya – Department of Chemistry and Biochemistry, California State University Northridge, 18111 Nordhoff St. Northridge, California 91330, USA

Christopher Pakhanyan – Department of Chemistry and Biochemistry, California State University Northridge, 18111 Nordhoff St. Northridge, California 91330, USA
Farid El Gabaly – Sandia National Laboratories, Livermore, California 94550, USA
Saori Kawaguchi-Imada – Super Photon ring-8, 1-1-1 Kouto, Sayo-cho – Sayo-gun Hyogo 679-5198 Japan
Jinghua Guo – Advanced Light Source, Lawrence Berkeley National Laboratory, Berkeley, California 94720 , USA
Zengqing Zhuo – Advanced Light Source, Lawrence Berkeley National Laboratory, Berkeley, California 94720 , USA
Min-Jae Kim – Advanced Light Source, Lawrence Berkeley National Laboratory, Berkeley, California 94720 , USA
Blake Sturtevant – Los Alamos National Laboratory, Los Alamos, New Mexico 87545, USA
Joseph A. Teprovich Jr. – Department of Chemistry and Biochemistry, California State University Northridge, 18111 Nordhoff St. Northridge, California 91330, USA
Mark D. Allendorf – Sandia National Laboratories, Livermore, California 94550, USA

Author Contributions

The manuscript was written through contributions of all authors. All authors have given approval to the final version of the manuscript.

ACKNOWLEDGMENTS

We thank Prof. Russell J. Hemley and Mr. Abdul Haseeb Manayil Marathamkottil for helpful discussions. Sandia National Laboratories is a multi-mission laboratory managed and operated by National Technology & Engineering Solutions of Sandia, LLC (NTESS), a wholly owned subsidiary of Honeywell International Inc., for the U.S. Department of Energy's National Nuclear Security Administration (DOE/NNSA) under contract DE-NA0003525. This work was supported by the Sandia Laboratory Directed Research and Development Program. Los Alamos National Laboratory, an affirmative action equal opportunity employer, is managed by Triad National Security, LLC for the U.S. Department of Energy's NNSA, under contract 89233218CNA000001. Synchrotron XRD measurements were supported by the Japan Synchrotron Radiation Research Institute (JASRI) (Proposal No. 2023B1271). This research used resources of the Advanced Light

Source, which is a DOE Office of Science User Facility under contract no. DE-AC02-05CH11231. This paper describes objective technical results and analysis. Any subjective views or opinions that might be expressed in this paper do not necessarily represent the views of the U.S. Department of Energy or the United States Government.

REFERENCES:

(1) Allendorf, M. D.; Stavila, V.; Snider, J. L.; Witman, M.; Bowden, M. E.; Brooks, K.; Tran, B. L.; Autrey, T. Challenges to developing materials for the transport and storage of hydrogen. *Nat. Chem.* **2022**, *14*, 1214-1223.

(2) Corgnale, C.; Hardy, B.; Motyka, T.; Zidan, R.; Teprovich, J.; Peters, B. Screening analysis of metal hydride based thermal energy storage systems for concentrating solar power plants. *Renew. Sustain. Energy Rev* **2014**, *38*, 821-833.

(3) Oumellal, Y.; Rougier, A.; Nazri, G. A.; Tarascon, J. M.; Aymard, L. Metal hydrides for lithium-ion batteries. *Nat. Mater.* **2008**, *7*, 916-921.

(4) Mohtadi, R.; Orimo, S. The renaissance of hydrides as energy materials. *Nat. Rev. Mater.* **2016**, *2*, 16091.

(5) Bos, W. G.; Gayer, K. H. The rare earth hydrides. *J. Nucl. Mater.* **1966**, *18*, 1-30.

(6) Sarma, A. C.; Bos, W. G. The LIII X-ray emission edge in lanthanum hydrides. *J. Phys. Chem. Solids* **1971**, *32*, 1423-1428.

(7) Huiberts, J. N.; Griessen, R.; Rector, J. H.; Wijngaarden, R. J.; et al. Yttrium and lanthanum hydride films with switchable optical properties. *Nature* **1996**, *380*, 231-236.

(8) Udovic, T. J.; Huang, Q.; Karmonik, C.; Rush, J. J. Structural ordering and dynamics of LaH_{3-x}. *J. Alloys Comp.* **1999**, *293-295*, 113-117.

(9) Bischof, R.; Kaldis, E.; Tellefsen, M. Crystal growth and phase diagram of lanthanum trihydride, LaH_{3-x}. *Journal of Crystal Growth* **1984**, *70*, 491-496.

(10) Giorgi, T. A.; Ferrario, B.; Storey, B. An updated review of getters and gettering. *Journal of Vacuum Science & Technology A* **1985**, *3*, 417-423.

(11) Kutyla, C.; Bessouet, C.; Lemettre, S.; Leroy, L.; Bosseboeuf, A.; Coste, P.; Sauvage, T.; Wendling, O.; Bellamy, A.; Jagtap, P.; Escoubas, S.; Guichet, C.; Thomas, O.; Moulin, J. Hydrogen sorption in yttrium-based getter thin films. *Vacuum* **2023**, *207*, 111655.

(12) Dubey, S. K.; Ravi Kumar, K.; Tiwari, V.; Srivastva, U. Impacts, Barriers, and Future Prospective of Metal Hydride-Based Thermochemical Energy Storage System for High-Temperature Applications: A Comprehensive Review. *Energy Technology* **2024**, *12*, 2300768.

(13) Adams, M.; Buckley, C. E.; Busch, M.; Bunzel, R.; Felderhoff, M.; Heo, T. W.; Humphries, T. D.; Jensen, T. R.; Klug, J.; Klug, K. H.; Møller, K. T.; Paskevicius, M.; Peil, S.; Peinecke, K.; Sheppard, D. A.; Stuart, A. D.; Urbanczyk, R.; Wang, F.; Walker, G. S.; Wood, B. C.; et al. Hydride-based thermal energy storage. *Progress in Energy* **2022**, *4*, 032008.

(14) Drozdov, A. P.; Kong, P. P.; Minkov, V. S.; Besedin, S. P.; Kuzovnikov, M. A.; Mozaffari, S.; Balicas, L.; Balakirev, F. F.; Graf, D. E.; Prakapenka, V. B.; Greenberg, E.; Knyazev, D. A.; Tkacz, M.; Eremets, M. I. Superconductivity at 250 K in lanthanum hydride under high pressures. *Nature* **2019**, *569*, 528-531.

(15) Ashcroft, N. W. Hydrogen Dominant Metallic Alloys: High Temperature Superconductors? *Phys. Rev. Lett.* **2004**, *92*, 187002.

(16) Ashcroft, N. W. Metallic Hydrogen: A High-Temperature Superconductor? *Phys. Rev. Lett.* **1968**, *21*, 1748-1749.

(17) Pickard, C. J.; Errea, I.; Eremets, M. I. Superconducting Hydrides Under Pressure. *Annual Review of Condensed Matter Physics* **2020**, *11*, 57-76.

(18) Somayazulu, M.; Ahart, M.; Mishra, A. K.; Geballe, Z. M.; Baldini, M.; Meng, Y.; Struzhkin, V. V.; Hemley, R. J. Evidence for Superconductivity above 260 K in Lanthanum Superhydride at Megabar Pressures. *Phys. Rev. Lett.* **2019**, *122*, 027001.

(19) Li, X.; Huang, X.; Duan, D.; Pickard, C. J.; Zhou, D.; Xie, H.; Zhuang, Q.; Huang, Y.; Zhou, Q.; Liu, B.; Cui, T. Polyhydride CeH9 with an atomic-like hydrogen clathrate structure. *Nat. Commun.* **2019**, *10*, 3461.

(20) Kong, P.; Minkov, V. S.; Kuzovnikov, M. A.; Drozdov, A. P.; Besedin, S. P.; Mozaffari, S.; Balicas, L.; Balakirev, F. F.; Prakapenka, V. B.; Chariton, S.; Knyazev, D. A.; Greenberg, E.; Eremets, M. I. Superconductivity up to 243 K in the yttrium-hydrogen system under high pressure. *Nat. Commun.* **2021**, *12*, 5075.

(21) Wang, C.; Yi, S.; Cho, J.-H. Multiband nature of room-temperature superconductivity in LaH_{10} at high pressure. *Phys. Rev. B* **2020**, *101*, 104506.

(22) Fang Hong, L. Y., Pengfei Shan, Pengtao Yang, Ziyi Liu, Jianping Sun, Yunyu Yin, Xiaohui Yu, Jinguang Cheng,; Zhao, Z. Superconductivity of Lanthanum Superhydride Investigated Using the Standard Four-Probe Configuration under High Pressures. *Chin. Phys. Lett.* **2020**, *37*, 107401.

(23) Sun, D.; Minkov, V. S.; Mozaffari, S.; Sun, Y.; Ma, Y.; Chariton, S.; Prakapenka, V. B.; Eremets, M. I.; Balicas, L.; Balakirev, F. F. High-temperature superconductivity on the verge of a structural instability in lanthanum superhydride. *Nat. Commun.* **2021**, *12*, 6863.

(24) Cho, Y.; Cho, H.; Cho, E. S. Nanointerface Engineering of Metal Hydrides for Advanced Hydrogen Storage. *Chem. Mater.* **2023**, *35*, 366-385.

(25) Cho, Y.; Li, S.; Snider, J. L.; Marple, M. A. T.; Strange, N. A.; Sugar, J. D.; El Gabaly, F.; Schneemann, A.; Kang, S.; Kang, M.-h.; Park, H.; Park, J.; Wan, L. F.; Mason, H. E.; Allendorf, M. D.; Wood, B. C.; Cho, E. S.; Stavila, V. Reversing the Irreversible: Thermodynamic Stabilization of $LiAlH_4$ Nanoconfined Within a Nitrogen-Doped Carbon Host. *ACS Nano* **2021**, *15*, 10163-10174.

(26) Stavila, V.; Li, S.; Dun, C.; Marple, M. A. T.; Mason, H. E.; Snider, J. L.; Reynolds, J. E., 3rd; El Gabaly, F.; Sugar, J. D.; Spataru, C. D.; Zhou, X.; Dizdar, B.; Majzoub, E. H.; Chatterjee, R.; Yano, J.; Schlomberg, H.; Lotsch, B. V.; Urban, J. J.; Wood, B. C.; Allendorf, M. D. Defying Thermodynamics: Stabilization of Alane Within Covalent Triazine Frameworks for Reversible Hydrogen Storage. *Angew. Chem. Int. Ed.* **2021**, *60*, 25815-25824.

(27) Bartenbach, D.; Wenzel, O.; Popescu, R.; Faden, L. P.; Reiss, A.; Kaiser, M.; Zimina, A.; Grunwaldt, J. D.; Gerthsen, D.; Feldmann, C. Liquid-Phase Synthesis of Highly Reactive Rare-Earth Metal Nanoparticles. *Angew. Chem. Int. Ed.* **2021**, *60*, 17373-17377.

(28) Carr, C. L.; Jayawardana, W.; Zou, H.; White, J. L.; El Gabaly, F.; Conradi, M. S.; Stavila, V.; Allendorf, M. D.; Majzoub, E. H. Anomalous H2 Desorption Rate of $NaAlH_4$ Confined in Nitrogen-Doped Nanoporous Carbon Frameworks. *Chem. Mater.* **2018**, *30*, 2930-2938.

(29) Lezanska, M.; Pietrzyk, P.; Sojka, Z. Investigations into the Structure of Nitrogen-Containing CMK-3 and OCM-0.75 Carbon Replicas and the Nature of Surface Functional Groups by Spectroscopic and Sorption Techniques. *J. Phys. Chem. C* **2010**, *114*, 1208-1216.

(30) Sainio, S.; Wester, N.; Aarva, A.; Titus, C. J.; Nordlund, D.; Kauppinen, E. I.; Leppänen, E.; Palomäki, T.; Koehne, J. E.; Pitkänen, O.; Kordas, K.; Kim, M.; Lipsanen, H.; Mozetič, M.; Caro, M. A.; Meyyappan, M.; Koskinen, J.; Laurila, T. Trends in Carbon, Oxygen, and Nitrogen Core in the X-ray Absorption Spectroscopy of Carbon Nanomaterials: A Guide for the Perplexed. *J. Phys. Chem. C* **2021**, *125*, 973-988.

(31) Lawley, C.; Arab, A.; Hartl, A.; Staykov, A.; Döbeli, M.; Schmitt, T.; Pergolesi, D.; Lippert, T.; Strocov, V. N. Momentum-resolved electronic structure of $LaTiO_2N$ photocatalysts by resonant Soft-X-ray ARPES. *Commun. Mater.* **2023**, *4*, 15.

(32) Hirao, N.; Kawaguchi, S. I.; Hirose, K.; Shimizu, K.; Ohtani, E.; Ohishi, Y. New developments in high-pressure X-ray diffraction beamline for diamond anvil cell at SPring-8. *Matter Radiat. Extremes* **2020**, *5*, 018403.

(33) Nylén, J.; Sato, T.; Soignard, E.; Yarger, J. L.; Stoyanov, E.; Häussermann, U. Thermal decomposition of ammonia borane at high pressures. *J. Chem. Phys.* **2009**, *131*, 104506.

(34) Lin, Y.; Mao, W. L.; Drozd, V.; Chen, J.; Daemen, L. L. Raman spectroscopy study of ammonia borane at high pressure. *J. Chem. Phys.* **2008**, *129*, 234509.

(35) Prescher, C.; Prakapenka, V. B. DIOPTAS: a program for reduction of two-dimensional X-ray diffraction data and data exploration. *High Pressure Res.*, **2015**, *35*, 223-230.

(36) Toby, B. H.; Von Dreele, R. B. GSAS-II: the genesis of a modern open-source all purpose crystallography software package. *J. Appl. Crystallogr* **2013**, *46*, 544-549.

(37) Laniel, D.; Trybel, F.; Winkler, B.; Knoop, F.; Fedotenko, T.; Khandarkhaeva, S.; Aslandukova, A.; Meier, T.; Chariton, S.; Glazyrin, K.; Milman, V.; Prakapenka, V.; Abrikosov, I. A.; Dubrovinsky, L.; Dubrovinskaia, N. High-pressure synthesis of seven lanthanum hydrides with a significant variability of hydrogen content. *Nat. Commun.* **2022**, *13*, 6987.

(38) Machida, A.; Watanuki, T.; Kawana, D.; Aoki, K. Phase separation of lanthanum hydride under high pressure. *Phys. Rev. B* **2011**, *83*, 054103.

(39) Chen, W.; Semenok, D. V.; Troyan, I. A.; Ivanova, A. G.; Huang, X.; Oganov, A. R.; Cui, T. Superconductivity and equation of state of lanthanum at megabar pressures. *Phys. Rev. B* **2020**, *102*, 134510.

(40) Kresse, G.; Furthmüller, J. Efficiency of ab-initio total energy calculations for metals and semiconductors using a plane-wave basis set. *Comp. Mater. Sci.* **1996**, *6*, 15-50.

(41) Blöchl, P. E. Projector augmented-wave method. *Phys. Rev. B* **1994**, *50*, 17953-17979.

(42) Schneemann, A.; Wan, L. F.; Lipton, A. S.; Liu, Y.-S.; Snider, J. L.; Baker, A. A.; Sugar, J. D.; Spataru, C. D.; Guo, J.; Autrey, T. S.; Jørgensen, M.; Jensen, T. R.; Wood, B. C.; Allendorf, M. D.; Stavila, V. Nanoconfinement of Molecular Magnesium Borohydride Captured in a Bipyridine-Functionalized Metal–Organic Framework. *ACS Nano* **2020**, *14*, 10294-10304.

(43) Comanescu, C. Graphene Supports for Metal Hydride and Energy Storage Applications. *Crystals*, **2023**, *13*, 878.

(44) Konarova, M.; Tanksale, A.; Norberto Beltramini, J.; Qing Lu, G. Effects of nano-confinement on the hydrogen desorption properties of MgH_2. *Nano Energy* **2013**, *2*, 98-104.

(45) Shinar, J.; Dehner, B.; Barnes, R. G.; Beaudry, B. J. Anomalous resistivity peaks, localization transitions, and the electronic structure of substoichiometric lanthanum trihydrides. *Phys. Rev. Lett.* **1990**, *64*, 563-566.

(46) Vajda, P.; Daou, J. N. Semiconductor-Metal-Semiconductor Transitions in the Superstoichiometric Dihydride YH_2.10. *Phys. Rev. Lett.* **1991**, *66*, 3176-3178.

(47) Wang, H.; Salzbrenner, P. T.; Errea, I.; Peng, F.; Lu, Z.; Liu, H.; Zhu, L.; Pickard, C. J.; Yao, Y. Quantum structural fluxion in superconducting lanthanum polyhydride. *Nat. Commun.* **2023**, *14*, 1674.

(48) Griessen, R.; Huiberts, J. N.; Kremers, M.; van Gogh, A. T. M.; Koeman, N. J.; Dekker, J. P.; Notten, P. H. L. Yttrium and lanthanum hydride films with switchable optical properties. *J. Alloys Comp.* **1997**, *253-254*, 44-50.

(49) Yan, C.; Wagner, M. J. Air- and Water-Stable Gold-Coated Gadolinium Metal Nanocrystals. *Nano Lett.* **2013**, *13*, 2611-2614.

TOC Figure

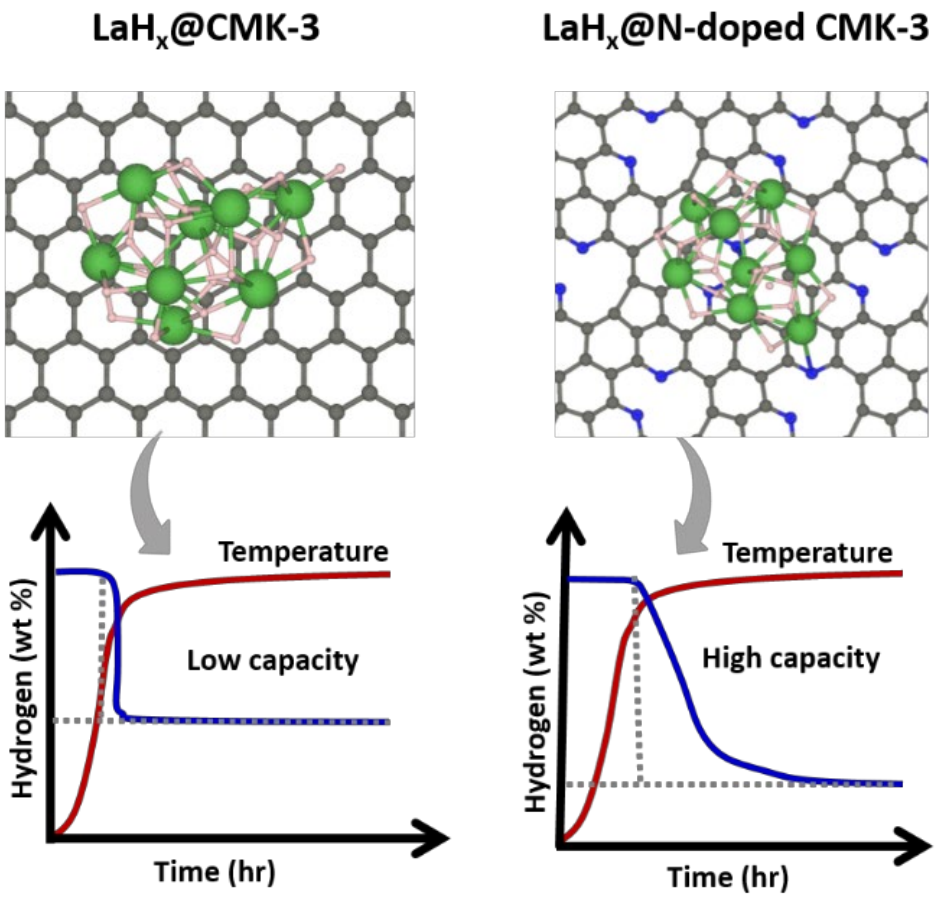
LaH$_x$@CMK-3
LaH$_x$@N-doped CMK-3
Temperature
Low capacity
Hydrogen (wt %)
Time (hr)
Temperature
High capacity
Hydrogen (wt %)
Time (hr)